An experimental and theoretical investigation of particle–wall impacts in a T-junction

D. Vigolo[1,†], **I. M. Griffiths**[2,‡,†], **S. Radl**[3] **and H. A. Stone**[1,†]

[1]Department of Mechanical and Aerospace Engineering, Princeton University, Princeton, NJ 08544, USA

[2]Mathematical Institute, 24–29 St Giles', University of Oxford, Oxford OX1 3LB, England, UK

[3]Institute for Process and Particle Engineering, Graz University of Technology, Inffeldgasse 13/III, 8010 Graz, Austria

Understanding the behaviour of particles entrained in a fluid flow upon changes in flow direction is crucial in problems where particle inertia is important, such as the erosion process in pipe bends. We present results on the impact of particles in a T-shaped channel in the laminar–turbulent transitional regime. The impacting event for a given system is described in terms of the Reynolds number and the particle Stokes number. Experimental results for the impact are compared with the trajectories predicted by theoretical particle-tracing models for a range of configurations to determine the role of the viscous boundary layer in retarding the particles and reducing the rate of collision with the substrate. In particular, a two-dimensional model based on a stagnation-point flow is used together with three-dimensional numerical simulations. We show how the simple two-dimensional model provides a tractable way of understanding the general collision behaviour, while more advanced three-dimensional simulations can be helpful in understanding the details of the flow.

Key words: multiphase and particle-laden flows, particle/fluid flow, pipe flow boundary layer

1. Introduction

When particles are dispersed in a fluid flowing in a channel, and the direction of motion changes abruptly, particle collisions with the constraining surface may occur. For instance, if we consider a pipe flow through an elbow or T-shaped section, where particles are dispersed in the fluid, particle inertia can play a role in leading to an impact that can potentially produce damage of the surface. Such solid particle erosion (SPE) is a well-known phenomenon in industrial piping systems (see, for example, Levy 1995). A wide range of experimental and computational studies have been performed on piping systems including both straight sections and bends to evaluate the damage caused by SPE. One such technique utilizes jet impingement on a surface in which, for example, the influence on the strike angle or substrate and erodent material may be considered. An alternative approach to study erosion at high impact speeds is

† Email addresses for correspondence: vigolo.daniele@gmail.com, ian.griffiths@maths.ox.ac.uk, hastone@princeton.edu

‡ The first two authors contributed equally to this work.

to perform a 'pot erosion test', in which a rotor spins in a pot filled with the slurry containing the erodent under investigation. A more detailed account of SPE work comprising experimental and computational approaches is presented in table 1.

In all of the indicated literature the principal goal is to evaluate the damage to the boundaries, and hence the results depend strongly on the chosen material and/or on the erosion model applied. In this paper we approach this problem in a more general way, by focusing experimentally and theoretically on the specific particle path towards the wall that leads to an impact, rather than the actual damage caused. In particular, we consider high-Reynolds-number laminar, particle-laden flows within a T-junction, which are characterized by the particle size and density, the details of the flow field and the system geometry. We evaluate particle trajectories by direct visualization of a range of experiments, and from their traces collect information on local direction and speed, final strike angle and position.

There is a wealth of literature describing the flow within similar geometries for a variety of Reynolds numbers, defined by $Re = \rho_f UL/\mu$, where ρ_f and μ denote the fluid density and viscosity, respectively, U the mean flow velocity and L the typical cross-section of the channel. However, the majority of this work focuses on much smaller devices, often with different arrangements of inlets and outlets, for example the flow in a microfluidic L-bend, T-channel or fork-shaped element (Haller, Woias & Kockmann 2009; Kockmann & Roberge 2011). The simplest study of particle collisions arises in the settling of dense particles in a static fluid. Such configurations allow the determination of the restitution coefficient, that is, the ratio between the rebound and the impact velocity (see, for example, Li, Hunt & Colonius 2012). These results are influenced by the type, asperity and shape of the surface and impacting particle (Sommerfeld & Huber 1999; Chun & Ladd 2006; Yang & Hunt 2008). The introduction of a flow field, as examined in this paper, clearly has a dramatic effect on the observed impact behaviour.

Early work in the area of inertial impactors (i.e. devices used for particle size analysis) attempted to identify the parameter space for which particles will impact a flat wall. In these studies, gas–particle flow through a nozzle with circular cross-section, or an infinitely long slit (i.e. the two-dimensional counterpart of the T-junction geometry considered in our work) has been analysed (Marple & Liu 1974; Rader & Marple 1985). This previous work isolated the particle Stokes number and the Reynolds number of the flow as the principal dimensionless parameters that dictate whether particles impact or not. However, Marple and coworkers did not determine a simple regime map for when particle–wall collisions occur, and focused on large density ratios $\rho = \rho_p/\rho_f$ only (ρ_p denotes the particle density). More recent work has considered the simulation of gas–particle flow in more complex three-dimensional geometries (see, for example, Vinchurkar, Longest & Peart 2009) although, again, simple regimes for particle–wall collisions have not been established.

Many studies consider the fluid mixing that arises in small T-shaped junctions where two miscible liquids enter the lateral branches of a T-junction, meeting and eventually mixing as they flow together in the converging channel towards the outlet (see, for example, Wong, Ward & Wharton 2004; Adeosun & Lawal 2009; Dreher, Kockmann & Woias 2009). Another flow configuration often used to study mixing phenomena is that in which the two inlets meet perpendicularly to each other at the T-junction and then move towards the outlet, which has been studied, for example, by Bruecker (1997) using three-dimensional particle image velocimetry. Although the geometry is essentially the same as the conventional T-junction we consider in this paper, the flow

Reference	Set-up	Erosion rate evaluation	Particle size (μm)	Particle material	Typical speed[a] (m s^{-1})	Type (E/C)[b]
Blanchard, Griffith & Rabinowicz (1984)	Elbows	Visual inspection, alternate layer of Cu and Ag	95–605	Sand	5	E
Benchaita, Griffith & Rabinowicz (1983)	Jet impingement (90°) on metallic plate	Surface profile by a 'pick up' needle system	200–1000	Sand	5.5–8	E/C
Shivamurthy et al. (2010)	Jet impingement (30°, 45°, 60°, 90°) on Stellite and Colmonoy	SEM images and weight loss measurement	100, 375	SiO_2	12	E
Zhao, Yamamoto & Matsumura (1995)	Jet impingement (90°) on steel	Surface profile and weight loss measurement	105, 149, 210	SiO_2	1.7	E
Zhang et al. (2007)	Jet impingement (90°)	Electrical resistance (ER) probe	25, 150	Sand	2.5, 5, 10	E/C
Lynn et al. (1991)	Erosion pot tester, particle in oil; evaluation of impact energy	SEM images	20–500	SiC	18.7	E
Clark (1991)	Erosion pot tester, water and water/glycerin mixture; viscosity dependence	SEM images	75–750	Glass	9.35, 18.7	E
Wood & Jones (2003)	Bends, straight section and jet impingement (90°)	Weight loss, profilometer and electrical resistance tomography (ERT) measurements	500–2000	Sand	0.5, 1, 1.5, 2, 2.5 Jet: 3.5	E
Levy, Jee & Yau (1987)	Jet impingement, slurry on steel; strike angle dependence	SEM images	44, 79	SiO_2, coal, SiC	10, 20, 30	E
Chen, McLaury & Shirazi (2006)	Plugged T-shaped channel and 90° elbow	Aluminium specimens checked by profilometer	150	Sand	3	E/C
McLaury et al. (1997)	Elbows and straight pipe	—	300	Sand	6	C

TABLE 1. Summary of significant work in the SPE literature. [a] Typical flow or particle velocity, [b] experimental (E) or computational (C) work.

configuration is completely different for mixing applications and particle–wall impacts are not considered.

The advent of greater computational power has enabled the recent extension of modelling techniques to general particle behaviour within turbulent flow regimes (see, for example, Guha 2008; Toschi & Bodenschatz 2009, for a comprehensive review). At high Reynolds numbers, in the range $8 \times 10^3 < Re < 1 \times 10^5$, experiments and simulations on impact and rebounding particles reveal that the particle behaviour and rebounding flow pattern near the wall is mainly dominated by particle inertia (Tu 2000; Tu *et al.* 2004).

The aim of our work here is to consider a scenario in which a dispersion of particles is made to flow in a high-Reynolds-number laminar flow while abruptly changing direction at a T-junction. The majority of the literature related to the study of similar flow regimes focuses attention on an inviscid flow (see, for example, Benchaita *et al.* 1983). Our paper extends the work in the field of particle impact to consider a spectrum of flow regimes in larger T-junction configurations that allow for the size of the viscous boundary layer, adjacent to the wall, to be non-negligible when compared with the size of a particle. Consequently, the viscous boundary layer may have an appreciable effect on the particle behaviour and impact dynamics. In addition we obtain insight into the key parameters that govern whether a particular configuration will generate wall impacts by considering a fully three-dimensional simulation of the flow behaviour. We exploit observations made about the flow field to derive a reduced two-dimensional model that is used to show that, for a given T-junction set-up, the system behaviour may be captured by three key dimensionless parameters, which describe respectively the flow field, the entrained-particle characteristics and the system geometry. The two-dimensional model is validated against both the three-dimensional simulations and the experimental observations. Finally, the theory is used to present phase diagrams that capture the features of any laminar flow field, viscous boundary layer and particle character to determine whether a system configuration will give rise to particle impacts, providing a significantly reduced characterization of this complex problem.

2. Experimental set-up

To study the influence of inertia on the particle–wall collisions, an aqueous dispersion of particles of different sizes and materials are injected into a flow in a transparent polycarbonate T-shaped channel with a square section of lateral dimensions $L = 0.48$ cm. In particular, we vary the particle-to-fluid density ratio in the range 1–4.5 by choosing beads made of polymethyl methacrylate (PMMA, with particle density $\rho_p = 1180$ kg m^{-3}), ordinary silica glass (SiO$_2$, $\rho_p = 2500$ kg m^{-3}), ZrO$_2$/SiO$_2$ glass ($\rho_p = 3800$ kg m^{-3}) and high-density barium titanate (TiBa) glass ($\rho_p = 4500$ kg m^{-3}). In addition, we cover more than an order of magnitude in particle radii ranging over $a = 10$–350 μm (see table 2). A sketch of the set-up used in the experiments is provided in figure 1(a). The flow is driven by a centrifugal pump (ViaAqua 3300) and the flow enters the device from the top and exits laterally via two outlets. Owing to the symmetry, the flow rate at one of the outlets is exactly half of the flow rate at the inlet.

The fluid used is a mixture of deionized water and glycerol (Sigma-Aldrich) in order to vary the viscosity (μ) and density (ρ_f) of the fluid to cover a wide range of
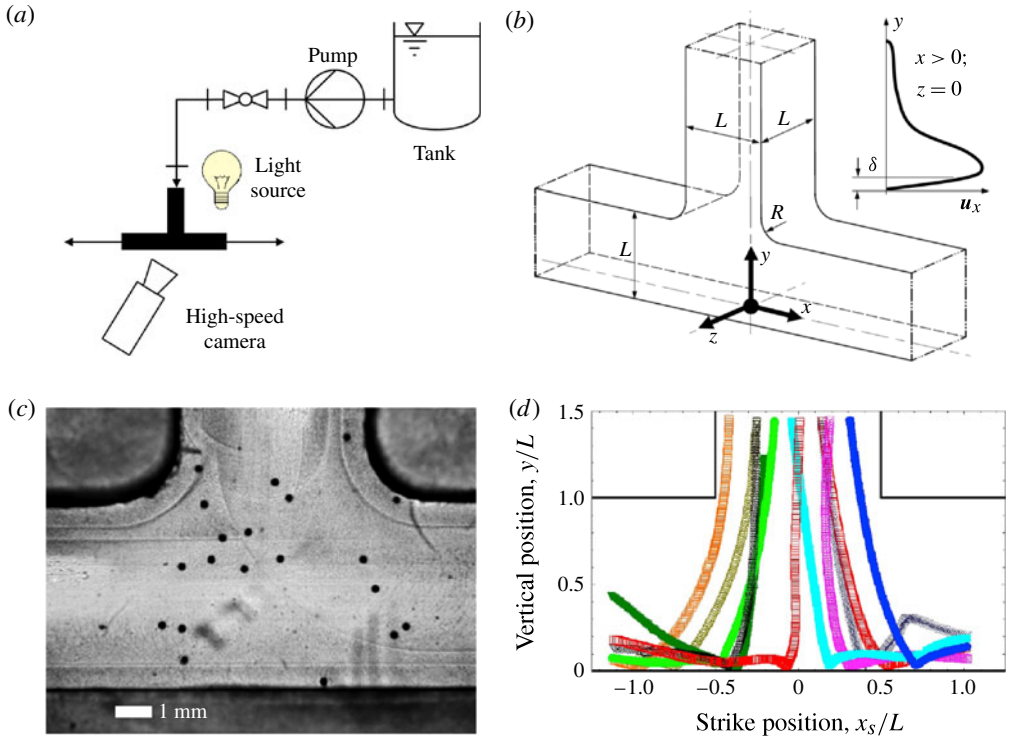
FIGURE 1. (Colour online) (*a*) A sketch of the experimental set-up. (*b*) A schematic of the T-shaped channel with the lateral size of the square-section channel, L, and the viscous boundary-layer thickness, δ. (*c*) A high-speed image of the impact zone where pure water is seeded with 97 μm radius TiBa glass particles ($Re = 6500$). (*d*) A plot showing a sequence of particle positions that depicts the trajectories of the impacting particles as obtained from the MATLAB routine.

Material	ρ_p (kg m^{-3})	a (μm)
Ti Ba glass [a]	4500	21, 50 [d], 69 [d], 97, 163 [d]
ZrO$_2$/SiO$_2$ [b]	3800	350
SiO$_2$ [b]	2500	75, 128, 175
PMMA [c]	1180	10

TABLE 2. Characteristics of the particles used in the experiments. [a] The particles were supplied by MO-SCI Specialty Products L.L.C., [b] the particles were supplied by GlenMills Inc., [c] the particles were supplied by Microbeads Spheromers CA 20, [d] the particle size tested but not shown in the experimental results below.

Reynolds numbers, Re, defined as

$$Re = \frac{\rho_f U L}{\mu}, \tag{2.1}$$

where U is the volume-averaged fluid velocity at the inlet. The glycerol–water ratios used, the respective densities and viscosities of the fluids, the average fluid speed that

Glycerol (%)	ρ_f (kg m^{-3})	μ (Pa s)	U^a (m s^{-1})	Re
0	997	0.00089	1.21	6500
10	1021	0.00114	1.17	5000
20	1045	0.0015	1.09	3600
30	1071	0.0021	1.06	2600
40	1097	0.0032	1.01	1700
50	1124	0.005	0.91	980
60	1151	0.0087	0.76	480
70	1178	0.017	0.47	160

TABLE 3. Characteristics of the fluid used in the experiments. [a] Average velocity corresponding to the highest flow rate achievable under these conditions.

could be attained at the highest flow rate and the associated channel Reynolds numbers are shown in table 3.

A typical experiment is conducted by recording high-speed images (up to 35 000 fps) of the impacting particles using a high-speed camera (Vision Research, Phantom v7.3) and by tracing the particle trajectories using an in-house MATLAB code. An example of the results obtained from the image analysis is given in figure 1(*d*), where we show the measured trajectories of an ensemble of particles impacting the bottom surface of the T-shaped channel. The particles may be traced by performing the experiments with the camera focused in the plane $z = 0$, i.e. at the centre of the channel. Our MATLAB routine is designed to track only particles that are perfectly in the focal plane and, as we are using an objective with a wide aperture (i.e. a Sigma 105 mm F2.8 EX DG Macro), the majority of the measured trajectories are based on particles that are exactly in the $z = 0$ plane. In our case the depth of field (DOF) can be evaluated with the following approximate formula valid for close-up imaging:

$$\text{DOF} \approx 2Nc\frac{m+1}{m^2} \tag{2.2}$$

where N is the f-number of the lens used, c is the so-called circle-of-confusion and m is the magnification of the lens. In our case $N = 2.8$, $c \approx 0.014$ mm (as the Phantom v7.3 camera we are using has a 17.6×13.2 mm^2 sensor size) and $m = 1$ for the macro lens we are using at the minimum focus distance. With these figures we obtain a DOF ≈ 0.16 mm.

Our particle-tracing approach provides two-dimensional information on the instantaneous position, speed, and direction of each particle and, in the case of a collision, it is possible to obtain information on the strike speed and angle. While we cannot measure the third (i.e. depth) component of the particle velocity (and, hence, the true strike angle), we argue that this velocity component is of relatively little importance, since the velocity components in the main flow direction are much larger than that in the spanwise direction. This feature is especially true when looking at the midplane of the T-junction, as shown in the next section.

A key parameter in determining the influence of hydrodynamic effects on whether a particle will impact a surface is the thickness of the viscous boundary layer on the lower boundary, which is given by $\delta = \sqrt{\mu/\rho_f \dot{\gamma}}$, where $\dot{\gamma}$ is the reference shear rate. While the shear rate will be a function of position in the T-junction, here we choose $\dot{\gamma} = U/L$, so that $\delta = L/\sqrt{Re}$ provides an approximate value for the boundary-layer thickness.

A second parameter in the problem is the ratio of the radius of an entrained particle, a, to the lateral size of the T-junction, L, which we define as $\epsilon = a/L$. In the experiments conducted here, ϵ is small and so the influence of the particle motion on the fluid flow is negligible. However, the ratio of the particle size to the boundary-layer thickness, α, is given by

$$\alpha = \frac{a}{\delta} = \epsilon \sqrt{Re}, \qquad (2.3)$$

which, since the Reynolds number can be large, is not necessarily small. In the experiments conducted here α ranges between 10^{-2} and 10, and thus the viscous boundary layer can have an appreciable effect on the particle trajectories.

3. Modelling strategy to derive the flow field

By performing direct numerical simulations (DNS) of the Navier–Stokes equations, we are able to obtain a detailed three-dimensional description of the flow field as a function of the Reynolds number. Since we are unable to measure accurately experimentally the particle motion in the direction of the channel's depth, this approach provides a better understanding for the detailed flow field and particle trajectories. In addition, we exploit observations from the simulations that allow us to develop a simplified two-dimensional model.

We study a dimensionless system, whereby lengths are non-dimensionalized with the lateral pipe size, L, velocities with the average fluid velocity, U, and time with L/U. The corresponding dimensional quantities (indicated by an asterisk) are

$$\boldsymbol{x}^* = L\boldsymbol{x}, \quad \boldsymbol{u}^* = U\boldsymbol{u}, \quad t^* = \frac{L}{U}t. \qquad (3.1)$$

In the following subsections, we present the three-dimensional modelling approach and the reduced two-dimensional model used to describe the flow field.

3.1. *Three-dimensional modelling*

First, three-dimensional simulations were performed using OpenFOAM, an open-source, transient numerical algorithm to solve the Navier–Stokes equations for an incompressible fluid flow. A suitably fine computational grid (1.4 million cells) was employed to ensure appropriate resolution of the boundary layer near the impacting region of the incoming fluid. The details of this numerical approach are summarized in the Appendix.

Typical streamlines based on the results of the numerical simulations are sketched in figure 2(a), which illustrate the complex (laminar) flow features that develop at even moderately large Reynolds numbers. The swirl of the flow in the form of two counter-rotating vortices increases gradually with increasing Reynolds number and the flow becomes more complex, with two large vortices arising near the impingement region and two smaller vortices above them (see figure 2a). The highest streamwise velocity in the centre plane ($z = 0$) is located in the range of $x = 0.8$ and $x = 1.1$. The location of the highest streamwise velocity moves closer to the wall (and, hence, the characteristic boundary-layer thickness decreases) with increasing Re (see figure 3(f) for a comparison of the velocity profiles at $x = 0.8$). For Reynolds numbers $Re \lesssim 540$, fluid parcels initially in the plane $z = 0$ remain in the plane, i.e. the z-component of the fluid velocity is zero, and the flow is approximately symmetric about the xy-plane, see, for example, figure 2(b). Furthermore, the streamlines in the three-dimensional simulations suggest that those particles that lie in the plane $z = 0$ are the most likely
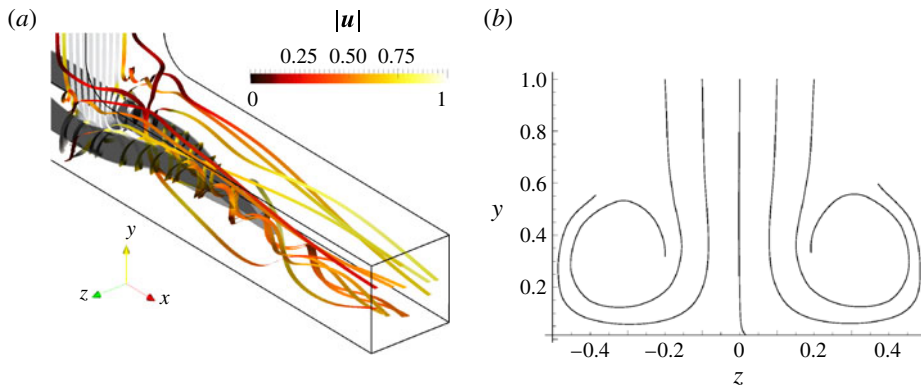
FIGURE 2. (Colour online) (*a*) Three-dimensional streamlines (coloured by the magnitude of the fluid velocity) and isocontours of the pressure field (shaded regions) based on a DNS of the flow in a T-junction ($Re = 500$). (*b*) Streamlines in the *yz*-plane of a T-junction.

to impact the lower surface, while particles out of this plane will become entrained in vortices. These features motivate our simplified model in the next section.

The flow pattern in the plane $z = 0$ is shown for various Reynolds numbers in figure 3. At low Reynolds numbers, for example $Re = 10$ (figure 3*a*), streamlines are parallel and the velocity profile in the two outlet channels is nearly symmetric. For Reynolds numbers up to $Re = 540$, we observe a steady flow (see results for $Re = 100$ and 500 in figure 3(*b*,*c*). In figure 3(*d*,*e*) typical results for an unsteady flow behaviour are shown. Clearly, streamlines originating at $z > 0$ are then able to cross the *xy*-midplane of the channel and velocity fluctuations are generally $O(1)$.

Despite the many complex flow features uncovered by the Navier–Stokes solver, it is clear from the simulations (figure 2*b*) that considering particles in the plane $z = 0$ will capture the most significant dynamical information on particles that are most likely to impact the lower wall of the T-junction, up to moderately high Reynolds numbers. These simulations motivate us to examine a reduced, tractable two-dimensional formulation of the system that is more amenable to parameter analysis. In the following subsection we establish a simpler two-dimensional model, where we also neglect the presence of the lateral walls. Our model will allow us to obtain a limit curve that separates the parameter regime where particle–wall collisions occur from that where no collisions are observed.

3.2. *Two-dimensional modelling*

In reducing the dimensionality of the system to focus on the particles in the $z = 0$ plane, which are most likely to impact on the channel wall, we may approximate the T-junction flow as a two-dimensional extensional flow in the *xy*-plane (see figure 1*b* for the coordinate geometry). In this model, we assume that the flow field near the lower boundary may be approximated by a stagnation-point flow, as studied, for example, by Benchaita *et al.* (1983). However, unlike in this work where the size of the viscous boundary layer is assumed to be small in comparison with the particle size, here we cannot neglect the effect of the viscous boundary layer. We therefore consider a model that also incorporates this effect and investigate the implications and results of this flow feature on the predicted particle behaviour. However, as discussed in §2,
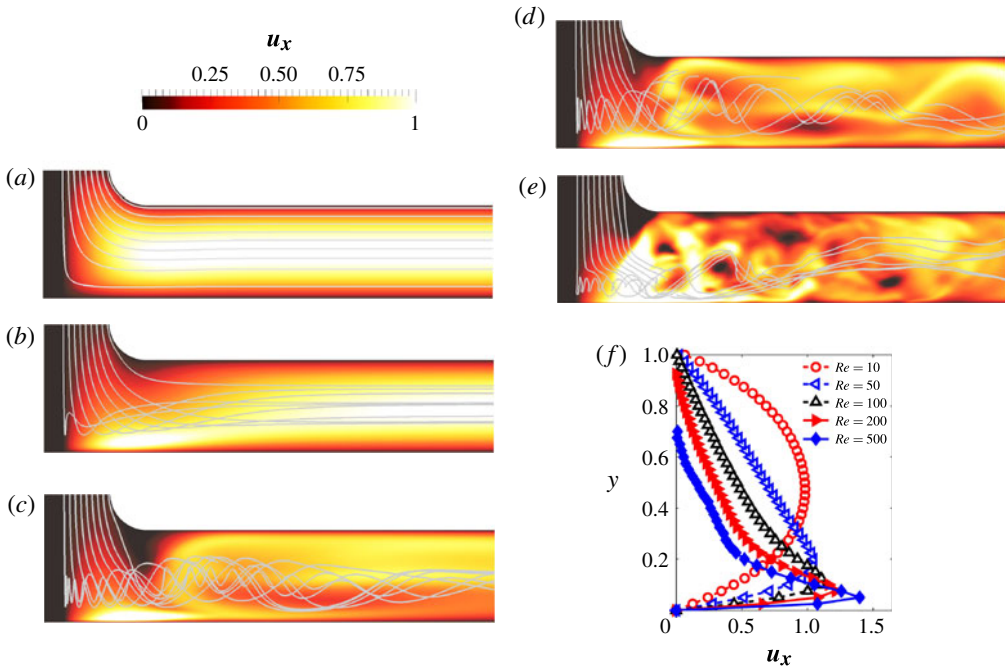
FIGURE 3. (Colour online) Contour plot of the instantaneous streamwise (i.e. x) velocity component at the centre of the channel ($z = 0$), as well as streamlines starting at $z = 0.3$ for various Reynolds numbers (streamlines in (d,e) piercing the plane $z = 0$ are not shown): (a) $Re = 10$; (b) $Re = 100$; (c) $Re = 500$; (d) $Re = 600$; (e) $Re = 2000$. (f) Velocity profile at $x = 0.8$, $z = 0$.

since the particles are much smaller than the channel geometry (i.e. $\epsilon \ll 1$) we assume they will not influence the fluid flow.

We assume that particles enter the midplane $z = 0$ at position $\boldsymbol{x}_0 = (x_0, y_0)$ in Cartesian coordinates into a viscous two-dimensional stagnation-point flow, which is given by the Hiemenz solution (Hiemenz 1911),

$$u = xf'\left(\sqrt{Re}y\right), \quad v = -\frac{1}{\sqrt{Re}}f\left(\sqrt{Re}y\right), \quad (3.2)$$

where f satisfies (primes denote derivatives)

$$f''' + ff'' - (f')^2 + 1 = 0, \quad (3.3a)$$

$$f(0) = f'(0) = 0, \quad f' \to 1 \text{ as } y \to \infty. \quad (3.3b)$$

The Reynolds number represents a measure of the relative thickness of the viscous boundary layer, which scales with $1/\sqrt{Re}$ as displayed in figure 4. As $y \to \infty$, $u \to x$ and $v \to -y$ which corresponds to the solution for an inviscid stagnation-point flow. We assume that the particles enter with velocity $\boldsymbol{u}_0 = (0, v_0(x_0, y_0))$, where $v_0 < 0$. The choice of the parameter y_0 corresponds to the entry point for the particles and here we choose $y_0 = 1$ so that the effect of the stagnation-point flow is observed at a distance of one pipe cross-sectional length from the impacting wall (this value is also taken by Benchaita *et al.* (1983)). We note that the Hiemenz solution equation (3.2) for the flow field may be generalized to three dimensions by the Homann flow
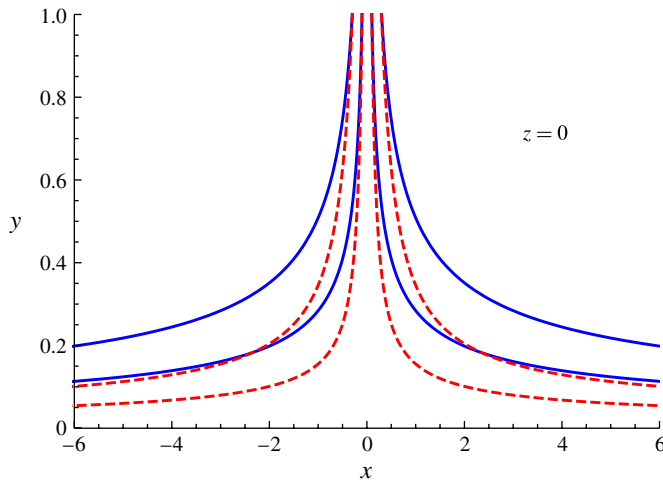
FIGURE 4. (Colour online) Streamlines for the Hiemenz viscous stagnation-point flow (3.2) for $Re = 1$ (solid, shown in blue online) and $Re = 100$ (dashed, shown in red online), which illustrates the effect of the viscous boundary layer.

solution (Homann 1936), but here we are concerned only with the two-dimensional solution, which captures the flow behaviour relevant to our analysis of impact.

4. Particle trajectories

There are various forces that contribute to the motion of the particles suspended in a flowing fluid. Whilst the viscous drag force will tend to guide particles along streamlines, other forces, for example those arising as a result of particle inertia and lift, will cause the particles to deviate from the streamlines. As a result, appropriate force models must be chosen since we cannot resolve the details of the flow around individual particles. There are several potentially relevant forces that we detail below.

The principal force exerted on a particle is the drag due to the viscous resistance of the surrounding fluid. Specifically, for a given flow field the particles experience a dimensional drag force, $\boldsymbol{F}_D^*$ (where we recall that $*$ denotes a dimensional quantity), which we assume to be (approximately) quadratic in nature, as in Benchaita *et al.* (1983),

$$\boldsymbol{F}_D^* = \frac{C_D}{2}\rho_f \pi a^2 (\boldsymbol{u}^* - \dot{\boldsymbol{x}}_p^*)|\boldsymbol{u}^* - \dot{\boldsymbol{x}}_p^*|, \tag{4.1}$$

where $\boldsymbol{x}_p^*$ denotes the dimensional particle position, dots denote time derivatives and C_D is the drag coefficient. For example, the Khan–Richardson model expresses the force on a particle for a large dynamic range of Reynolds numbers, $10^{-2} < Re < 10^5$ (Richardson *et al.* 2002) and has the form

$$C_D = 2(1.849 Re_p^{-0.31} + 0.293 Re_p^{0.06})^{3.45}, \tag{4.2}$$

where Re_p is the particle Reynolds number, defined by

$$Re_p = \frac{2a\rho_f |\boldsymbol{u}^* - \dot{\boldsymbol{x}}_p^*|}{\mu}. \tag{4.3}$$

We may use this definition to allow us to write the particle Reynolds number in terms of the Reynolds number and the dimensionless fluid and particle velocity via

$$Re_p = 2\epsilon Re |\boldsymbol{u} - \dot{\boldsymbol{x}}_p|. \tag{4.4}$$

The dependence of the drag coefficient on the local particle and fluid velocity means that we first solve for the flow and then determine the drag coefficient, C_D, using (4.2) *a posteriori*.

Other potentially relevant forces experienced by the particles within the bulk fluid flow are: the drag due to a mean pressure gradient acting on the surface of the particle,

$$\boldsymbol{F}_p^* = -\tfrac{4}{3}\pi a^3 \boldsymbol{\nabla}^* p^*, \tag{4.5}$$

where p^* is the dimensional fluid pressure (Clift, Grace & Weber 1978); added mass forces, which originate from the acceleration of the surrounding fluid (Clift *et al.* 1978),

$$\boldsymbol{F}_a^* = \frac{2}{3}\pi a^3 \rho_f \frac{\mathrm{d}}{\mathrm{d}t^*}(\boldsymbol{u}^* - \dot{\boldsymbol{x}}_p^*); \tag{4.6}$$

lift due to stresses induced by fluid and/or particle rotation (Rubinow & Keller 1961),

$$\boldsymbol{F}_l^* = C_L \rho_f \pi a^3 (\boldsymbol{u}^* - \dot{\boldsymbol{x}}_p^*) \times \boldsymbol{\omega}^*, \tag{4.7}$$

where $\boldsymbol{\omega}^*$ is the angular velocity of the particle relative to the fluid and C_L is the corresponding lift coefficient; and gravity,

$$\boldsymbol{F}_g^* = \tfrac{4}{3}\pi a^3 (\rho_p - \rho_f)\boldsymbol{g}, \tag{4.8}$$

where $\boldsymbol{g}$ is the acceleration due to gravity.

As the particles approach the wall, they also experience lubrication forces due to the viscous flow between the particle surface and a surrounding surface, in both the normal and tangential directions to the wall. We determine the normal force experienced via the model proposed by (Goldman, Cox & Brenner 1967),

$$\boldsymbol{F}_n^* = -6\pi\mu a^2 \frac{\dot{y}_p^*}{(y_p^* - a)}\boldsymbol{e}_y, \tag{4.9}$$

where $\boldsymbol{e}_y$ denotes the unit vector in the y^*-direction, perpendicular to the wall. As $y_p^* \to a$ and the particle approaches the wall (recalling that $\boldsymbol{x}^*$ denotes the coordinate of the centre of the particle so when $y_p^* = a$ the particle is touching the wall), the normal force diverges, indicating that a particle can never strike a perfectly smooth wall. In practice, however, both the surfaces of the wall and the particle are not perfectly smooth. In our model we therefore classify a *strike* when the particle comes within a distance $y_p^* = a + b$, where b is a characteristic roughness of the wall (we assume the particles to be perfectly smooth here). The corresponding dimensionless parameter $\beta = b/L$ characterizes the roughness of the wall. However, in our experiments, since we are concerned only with the effect of varying the particle type within our T-junction set-up, this parameter is a constant for all experiments. The typical wall roughness of the polycarbonate channel used in our experiments is 5 μm, which leads to a roughness parameter $\beta = 1 \times 10^{-3}$ which we use for all our simulations.

The tangential force experienced by a particle in the proximity of a wall, $\boldsymbol{F}_t^*$, is approximated by (Pasol *et al.* 2011),

$$\boldsymbol{F}_t^* = -\frac{16\pi\mu a}{5} \log\left(\frac{a}{y_p^* - a}\right) \dot{x}_p^* \boldsymbol{e_x}, \tag{4.10}$$

when $y^* - a \ll a$ and the particle is much closer to the wall than its radius. Here $\boldsymbol{e_x}$ and $\boldsymbol{e_z}$ denote, respectively, unit vectors in the x^* and z^* directions. To ensure that this force tends to zero as we move away from the wall we use a suitable representation that captures the force close to the wall while matching to the required far-field behaviour, which leads to the uniformly valid tangential force

$$\boldsymbol{F}_{uni,t}^* = -\frac{16\pi\mu a}{5} \log\left(1 + \frac{a}{y_p^* - a}\right) \dot{x}_p^* \boldsymbol{e_x}. \tag{4.11}$$

The resulting dimensionless equation that governs the particle trajectories is thus given by

$$\begin{aligned}
St\,\ddot{\boldsymbol{x}}_p = {} & \frac{C_D}{2}(\boldsymbol{u} - \dot{\boldsymbol{x}}_p)|\boldsymbol{u} - \dot{\boldsymbol{x}}_p| - \frac{4}{3}\epsilon\nabla p + \frac{2}{3}\epsilon\frac{\mathrm{d}}{\mathrm{d}t}(\boldsymbol{u} - \dot{\boldsymbol{x}}_p) + \epsilon C_L(\boldsymbol{u} - \dot{\boldsymbol{x}}_p) \times \omega \\
& + \frac{4}{3}\frac{\epsilon}{Fr^2}\left(\frac{\rho_p}{\rho_f} - 1\right)\hat{\boldsymbol{g}} - \frac{6}{\sqrt{Re}}\frac{\dot{y}_p}{(\sqrt{Re}y_p - \alpha)}\boldsymbol{e_y} \\
& - \frac{16}{5\alpha\sqrt{Re}}\log\left(\frac{\sqrt{Re}y_p}{\sqrt{Re}y_p - \alpha}\right)\dot{x}_p\boldsymbol{e_x},
\end{aligned} \tag{4.12}$$

where p is the dimensionless fluid pressure, scaled with $\rho_f U^2$, and $\hat{\boldsymbol{g}}$ is a unit vector in the direction of gravity. Here we define

$$St = \frac{4}{3}\frac{\rho_p}{\rho_f}\frac{a}{L} \tag{4.13}$$

as a characteristic Stokes number that represents the ratio of particle inertia to the fluid drag force; particles deviate progressively from streamlines with increasing Stokes number. In (4.12) the parameter $Fr = U/\sqrt{Lg}$ is the Froude number and reflects the relative importance of inertial to gravity forces. Since $\epsilon \ll 1$ we neglect the force terms on the right-hand side corresponding to pressure, added mass, lift and gravity so that the important forces on the particle are only the drag force and the lubrication forces experienced by the particle in the proximity of an external wall.

As described above, the force relation (4.12) may be solved for a given flow field to determine the particle Reynolds number, and thus the drag coefficient via (4.2). Typical values of Re_p/Re in the regime we consider are in general $10^{-1} \lesssim Re_p/Re \lesssim 1$; figure 5 considers the variation of $|\boldsymbol{u} - \dot{\boldsymbol{x}}_p|$ with time for a sample particle trajectory in different flow fields as it transits the T-junction.

Recalling that the flow profile and drag coefficient depend only on Re, that we have neglected all terms involving ϵ, and that we consider a constant wall roughness β, we find that the trajectories of the particles depend on three independent parameters: Re, St and α, representing the effect of the surrounding flow field, the nature of the particles and the relationship between particle size and the flow conditions, respectively.

The particle trajectories are determined by solving (4.12) via an Adams–Bashforth multistep method in Mathematica®, with the flow conditions set by either the two-
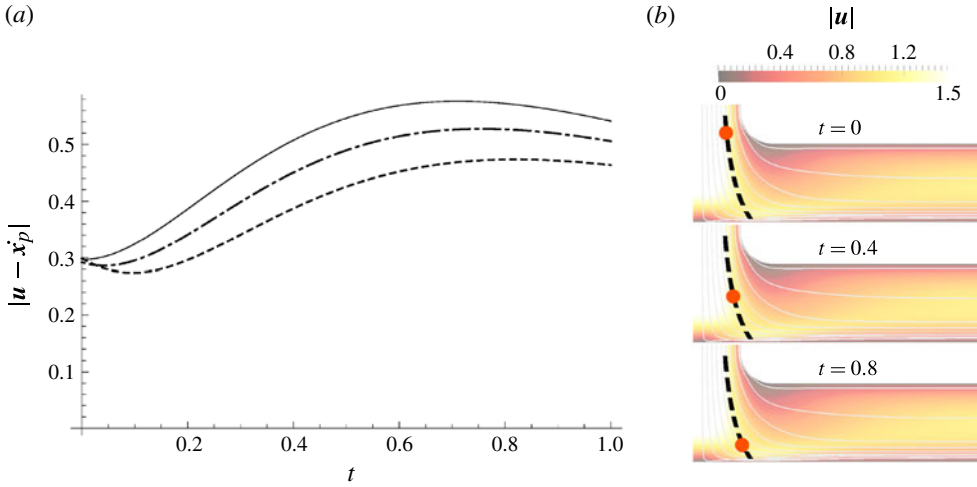
(*a*)

(*b*)

FIGURE 5. (Colour online) Plot of $|\boldsymbol{u} - \dot{\boldsymbol{x}}_p|$ versus t for a particle with $St = 0.35$ travelling in a flow characterized by $Re = 100$ in the presence of a viscous boundary layer with $\alpha = 0.9$ (dotted), 1 (dot-dashed) and 1.1 (solid). On the right-hand side we show a sketch of a particle following its trajectory (black dashed line) moving at a speed $\boldsymbol{x}_p$ while surrounded by a fluid flowing at a local velocity $\boldsymbol{u}$ (colour coded in the image), at three different times. The streamlines for the centre plane, $z = 0$, are also sketched (white solid lines).

dimensional Hiemenz stagnation-point flow model (3.2) or the flow profile obtained from the three-dimensional simulations. In both cases the particle tracing provides information on whether or not a dispersion of particles, characterized by their Stokes number, St, will collide with the bottom surface of a T-junction with wall roughness given by β, in a channel flow characterized by the Reynolds number, Re, and the ratio of the particle size to depth of the viscous boundary layer, α.

5. Model predictions

Before using the reduced two-dimensional model equations (3.2) and (4.12) to make predictions on the possibility of a collision we first validate the theory. This step is achieved by comparing the predictions on the effect of the viscous boundary layer with the results of two sets of experiments. First, we compare the predicted speed at impact versus the position of impact, and the corresponding experimental results obtained from the high-speed camera data as shown in figure 6(*b*). Both results show a strike velocity that increases monotonically with the strike position: $v_s \propto x_s^2$ for $|x_s| \lesssim L$ and $v_s \propto x_s$ for $|x_s| \gtrsim L$. Although the scaling of the impact velocity with the lateral (i.e. x) distance cannot be directly inferred from the flow data displayed in figures 3 and 4, a similar behaviour is expected considering the presence of the viscous boundary layer. Moreover, the theoretical and experimental predictions are in good agreement. We emphasize this agreement since the set-up comes with no fitting parameters, with all system parameters being determined explicitly for a given experiment.

Second, we find that the inclusion of the viscous boundary layer has a significant effect on the trajectories of particles that are comparable with or smaller than the thickness of the boundary layer, corresponding to solutions for which α is not too large. In figure 6(*c*) and its inset, we observe an approximately linear dependence of the impact position, x_s, on the initial position, x_0, of the particle. Cases are
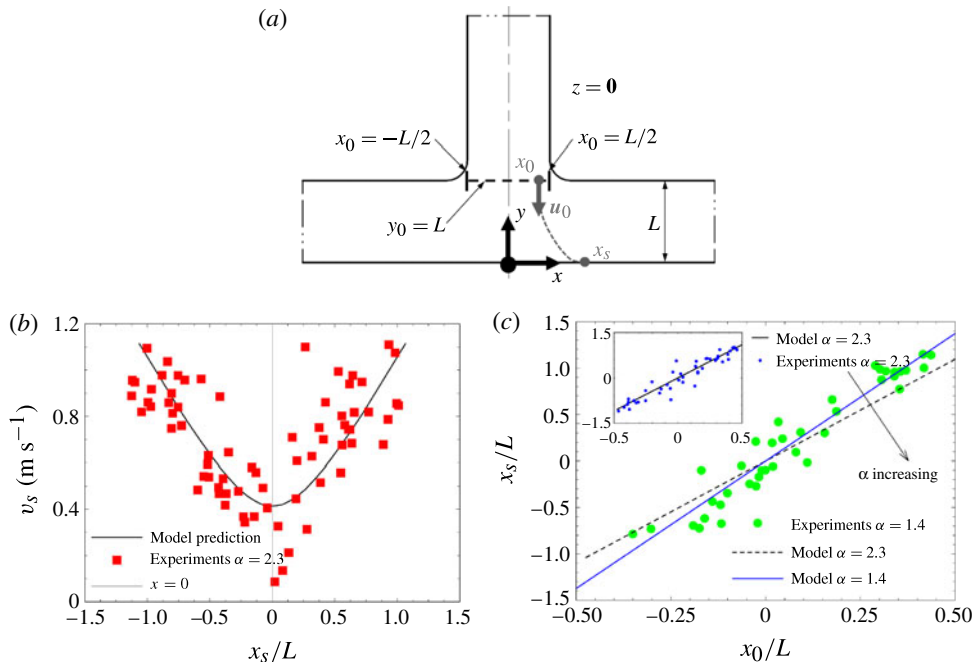
(*a*)

FIGURE 6. (Colour online) (*a*) Sketch of the T-junction, the coordinates for initial position, x_0, and strike position, x_s, are shown. (*b*) Wall impact speed, v_s, versus impact position, x_s, for $a = 97\ \mu\text{m}$ TiBa glass in pure water, $U = 1.2\ \text{m s}^{-1}$ ($Re = 6400$), $\alpha = 2.3$. (*c*) The dependence of the impact position, x_s, on the initial position, x_0, of the particle. The solid line indicates the model prediction and the symbols are experimental data; main plot: $a = 97\ \mu\text{m}$ TiBa glass in 70:30 water:glycerol mixture, $U = 1.06\ \text{m s}^{-1}$ ($Re = 2600$), $\alpha = 1.4$. Inset: $a = 97\ \mu\text{m}$ TiBa glass in pure water, $U = 1.2\ \text{m s}^{-1}$ ($Re = 3000$), $\alpha = 2.3$.

presented for two different values of α and, despite the experimental data being more scattered, good agreement with the theoretical predictions is still evident. In particular, as predicted by the theory, when α decreases the slope of the predicted curve and of the distribution of the experimental data points increases, which means that the presence of the viscous boundary layer changes the particles' trajectories and so results in impact positions more distant from the initial position at the inlet. As above, no fitting parameters were used in the comparison shown in the plot.

Having validated the mathematical model we now turn our attention to the dependence of the system behaviour on the dimensionless parameters that characterize the wall-impact problem. In figure 7(*a*) we present a phase-plane prediction in terms of the Stokes and Reynolds numbers. The results of the two-dimensional analysis illustrate an idealized divide into two zones: an 'impact zone', where particles will collide with the wall, and a 'non-impact zone', where particles injected into the flow will not touch the surface of the channel perpendicular to the inlet flow. The limit curve is validated by comparison with the more comprehensive three-dimensional simulations, which, for a given simulation, provides predicted points on this data curve, for $Re = 10$ and $Re = 100$ (shown by the + symbols). The agreement is excellent and, crucially, validates the predictions of the simplified two-dimensional model. It is clear that to determine the limit curve from three-dimensional simulations would require many simulations, being both computationally expensive and time consuming. We
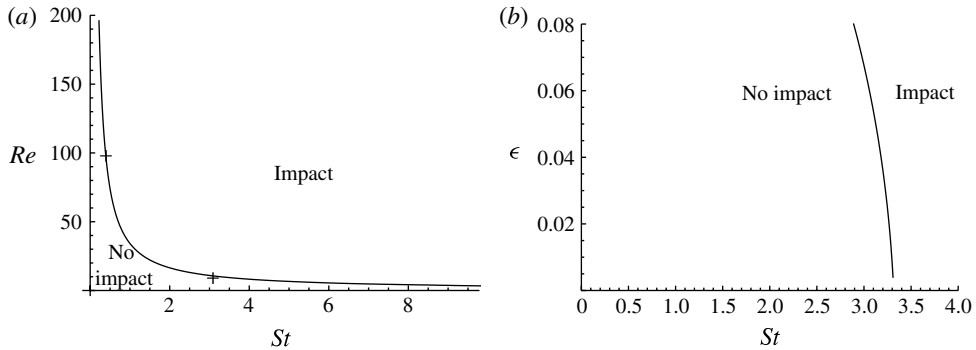
FIGURE 7. (*a*) Limiting curve in *Re*–*St* space dividing the impact and non-impact zone predicted by the two-dimensional Hiemenz flow field. The data points (+) show the limiting Stokes number for a given Reynolds number predicted by the fully three-dimensional model for simulations with $Re = 10$ and $Re = 100$. (*b*) Limiting curve in ϵ–*St* space divides the impact and non-impact zone (where $\epsilon = \alpha/\sqrt{Re}$ and $Re = 10$).

thus conclude that the two-dimensional model for particles within the two-dimensional Hiemenz viscous stagnation-point flow, (3.2), and the force-law (4.12), provides a simple way of determining the continuous limit curve that separates the regions of impact and non-impact of the entrained particles that is not offered by the full three-dimensional simulations or the corresponding experiments.

In figure 7(*b*) the two-dimensional theory is used to examine the effect of particle size on limit-curve prediction, by considering the dependence of $\epsilon = \alpha/\sqrt{Re}$ on *St*. This demonstrates that the particle size has only a weak influence on the impact predictions, which is consistent with our assumption that the particles do not influence the surrounding flow.

Finally, it only remains to compare the predictions made with the experimental data. The data is analysed via a MATLAB particle-tracing code to identify whether an impact occurs. From this data we define three categories for an individual particle's behaviour: 'impacting', when a particle clearly rebounds off the wall, that is, the rebound velocity away from the wall exceeds zero; 'not impacting', when a particle maintains a distance from the wall without collision; and 'barely impacting', when particles just graze the surface of the T-shaped channel and then proceed to the outlets.

In figure 8 we introduce the concept of impacting efficiency, E, to characterize more precisely the likelihood for particles to impact (under the assumption that particles are uniformly distributed over the inlet channel). Specifically, E is defined as the proportion of particles entering in a uniform distribution over $-1 \leqslant x \leqslant 1$ that impact on the channel wall. In particular, figure 8 shows the influence of the viscous boundary layer on the efficiency of the strike. The results generalize the work of Marple & Liu (1974) and Rader & Marple (1985) and corroborate a sharp transition from $E = 0$ to $E = 1$ as we vary *St* over a narrow range. As expected, an increase in the thickness of the viscous boundary-layer depth relative to the particle size (that is, with a decrease in α) leads to a decrease in the efficiency of strike. The steepness of these curves indicates that an empirical categorization of a flow configuration in which particles are impacting is only weakly dependent on the choice of the impacting efficiency, E, that is made. Indeed, the value of impacting efficiency chosen to separate the three classifications of impacting, barely impacting and not impacting was verified
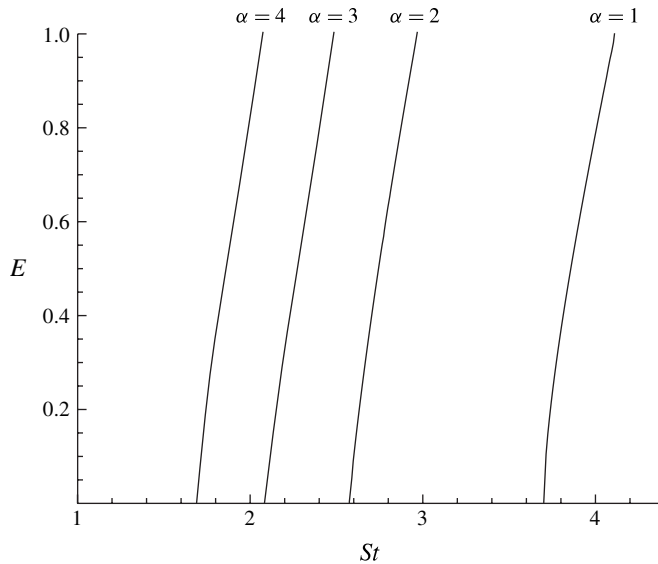
FIGURE 8. Impacting efficiency, E versus St for $\alpha = 1, 2, 3, 4$.

empirically via visual inspection of each movie to have only a weak effect. As a result, here we choose to categorize a complete system configuration as 'impacting' if the number of particles that are observed to rebound exceeds 25 % of the total (that is, an impacting efficiency, E, of 0.25), 'not impacting' if this ratio is less than 1 %, and 'barely impacting' for the region in between.

We use the observation of relative weak dependence of system behaviour upon particle size made in figure 7(b) to express Re in terms of α via the relation $\alpha = \epsilon\sqrt{Re}$, holding ϵ fixed. This allows the entire parametric dependence of the system to be collapsed onto a single phase plane for α versus St, using the two-dimensional flow equation (3.2) and (4.12), where the parameter α captures the effect of the viscous boundary layer and the flow regime. The resulting limiting curve predicted by the two-dimensional particle-tracing model is compared with the full set of experimental data in figure 9 with $\epsilon = 0.01$. The agreement between the two-dimensional model prediction and experimental results is extremely good, with any discrepancies most likely to be arising as a result of a combination of the three-dimensionality of the flow, which is reflected in the more complex three-dimensional numerical simulations, the level of ambiguity in classification of a strike from the experimental data, and the fact that some experiments may be taken slightly out of the $z = 0$ midplane. We thus conclude that the reduced two-dimensional viscous-flow model accurately captures the features required to determine whether a particle will impact on the channel wall.

These results thus suggest that this reduced two-dimensional analysis provides insight and a route to quick-scenario testing to determine whether or not an impact will occur for a range of applications. The results are particularly important in scenarios in which time constraints prohibit more lengthy full three-dimensional computational simulations, such as in situations where flow conditions are continuously being altered.
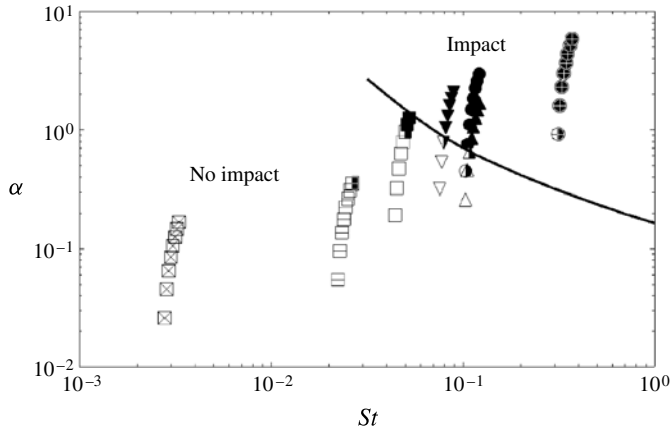
FIGURE 9. Phase plane α versus St. All of the experiments are divided into three main categories: particles 'impacting' (closed symbols), particle 'not impacting' (open symbols) and particle 'barely impacting' (half-filled symbols). The symbols identify the kind of particles used: $a = 10\,\mu m$ PMMA ($\boxtimes$), $a = 21\,\mu m$ TiBa ($\boxminus$), $a = 75\,\mu m$ SiO$_2$ ($\square$), $a = 97\,\mu m$ TiBa glass ($\triangle$), $a = 128\,\mu m$ SiO$_2$ ($\triangledown$), $a = 175\,\mu m$ SiO$_2$ ($\bigcirc$) and $a = 350\,\mu m$ ZrO$_2$/SiO$_2$ ($\oplus$). For each system investigated the figure shows seven experimental results obtained for water:glycerol ratios of 100:0, 90:10, 80:20, 70:30, 60:40, 50:50, 40:60 and 30:70. The solid line represents the two-dimensional model limiting curve that divides the phase plane into 'impact zone' and 'non-impact' zones. The theoretical curve is determined by fixing $\epsilon = 0.01$ and varying Re through $Re = (\alpha/\epsilon)^2$.

6. Closing remarks

The impact of particles entrained in a fluid with the wall in a T-shaped channel have been considered. A series of experiments were conducted for a broad range of system and particle configurations to investigate the effect of the presence of the viscous boundary layer on the resulting impacts on the channel.

Three-dimensional numerical simulations described the flow field and particle-tracing models enabled the tracking of entrained particles within the flow to determine those that will impact on the channel surface. By exploiting the system symmetry a simplified two-dimensional extensional-flow model was proposed. Comparison of this model with full three-dimensional simulations showed that the model characterizes the typical behaviour well and provides a tractable way of predicting the possibility of a collision for any given system configuration. The two-dimensional model was further validated by comparison with simple experimental observations and shown to agree well. The theory elucidated three key parameters on which the particle collisions depend: the Reynolds number, Re, which characterizes the flow field; the Stokes number, St, which describes the particle characteristics; and a parameter that relates the particle size to the depth of the viscous boundary layer, α.

We found that the regime of experimental interest gave rise only to a weak dependence of the system behaviour on the ratio of particle radius to T-junction cross-section. This allowed us to use the two-dimensional model to collapse the entire system behaviour onto a single phase plane for two parameters, α versus St. The result provides a continuous limiting curve that separates the phase space in which a particle and flow configuration would lead to an impact and those for which an impact would not occur, and the role of the viscous boundary layer in this behaviour.

The two-dimensional model thus provides a simple but accurate characterization of the behaviour of entrained particles that are most likely to impact on a channel wall within a T-junction flow.

The result of our work provides an easy tool to predict whether or not a particle will produce an impact and can be incorporated with a specific erosion model to determine the rate at which damage occurs. This study may be generalized to a range of situations involving a dispersion of particles in a constrained geometry.

The ability to assess the possible damage induced by SPE, especially in a sensitive environment such as the cooling pipe system of a nuclear power plant, where typically the coolant of the system cannot be replaced often, is crucial (Crockett & Horowitz 2010). Determining whether a flow field may be potentially dangerous in the presence of a dispersion of particles by simply evaluating a particular combination of dimensionless numbers represents a significant advantage over more complex computational fluid dynamics simulations. In particular, the reduced two-dimensional model presented here provides a limiting curve that immediately identifies the region of potential danger. Thus, such models provide a route to quick-scenario testing that is not offered by three-dimensional simulations, which require long computational time and are discrete, providing only information for a single, specific condition. Knowing the complete impact phase plane greatly simplifies the task of risk evaluation in scenarios where changes in the operating conditions render long computations impractical.

Acknowledgements

Appendix. Three-dimensional numerical simulations

We performed computational studies of single-phase flow in a T-junction using a finite-volume Navier–Stokes solver on unstructured meshes. Such solvers are a standard tool, e.g. for the analysis of the flow in microreactors (Kockmann & Roberge 2011). We used the open-source package OpenFOAM (Jasak 1996), which is widely used in industry and academia, and has demonstrated its parallel performance on various large-scale computer clusters. OpenFOAM can be seen as a mature tool for DNS of fluid flows in complex geometries, e.g. it has been applied recently to study turbulent channel flows (van Haren 2011). As DNS aims to resolve all details of the flow, it requires an extremely high spatial and temporal resolution during the numerical simulation. Specifically, we tested various computational grids for the flow at $Re = 600$, with cell counts between 375 000 and 2 million cells, with refined grids near the walls to capture the large gradients of the streamwise velocity component especially near the bottom wall. Also, a small enough time step was used to ensure a Courant number of $Co < 0.3$ in order to accurately capture the transients of the flow. These settings lead to typical simulation times of $O(10)$ days for $O(100)$ dimensionless time units that are needed to obtain a sufficiently large data set to

characterize unsteady flow features (steady flow was observed up to $Re \approx 540$). All simulations were performed in parallel on a Quad-Core CPU cluster. Based on our results for various grid spacings and numerical settings, we are confident that the results of our DNS for flows in T-junctions up to $Re = 600$ are independent of numerical resolution effects within an error tolerance of approximately 5 %. DNS results reported for higher Reynolds numbers are connected to somewhat larger inaccuracies, since the boundary-layer thickness becomes smaller and discretization errors increase.

Our DNS were used (i) to obtain a qualitative understanding of the flow field (an example is shown in figure 2(*a*)) and (ii) to extract data (instantaneous and time-averaged pressure and velocity distributions) for each point in the three-dimensional computational domain. The latter was realized by extracting the results in two-dimensional slices, and subsequently resampling the data on a regular grid in MATLAB; sampling was performed using MATLAB's '*griddata*' functionality using spline interpolation. The data was then imported into Mathematica® to track particles dispersed in the flow as described in § 4.

REFERENCES

ADEOSUN, J. T. & LAWAL, A. 2009 Numerical and experimental studies of mixing characteristics in a T-junction microchannel using residence-time distribution. *Chem. Engng Sci.* **64**, 2422–2432.

BENCHAITA, M. T., GRIFFITH, P. & RABINOWICZ, E. 1983 Erosion of metallic plate by solid particles entrained in a liquid jet. *J. Eng. Ind. (Trans. ASME)* **105**, 215–222.

BLANCHARD, D. J., GRIFFITH, P. & RABINOWICZ, E. 1984 Erosion of a pipe bend by solid particles entrained in water. *J. Eng. Ind. (Trans. ASME)* **106**, 213–221.

BRUECKER, C. 1997 Study of the three-dimensional flow in a T-junction using a dual-scanning method for three-dimensional scanning-particle-image velocimetry (3-D SPIV). *Exp. Therm. Fluid Sci.* **14**, 35–44.

CHEN, X., MCLAURY, B. S. & SHIRAZI, S. A. 2006 Numerical and experimental investigation of the relative erosion severity between plugged tees and elbows in dilute gas/solid two-phase flow. *Wear* **261**, 715–729.

CHUN, B. & LADD, A.J.C. 2006 Inertial migration of neutrally buoyant particles in a square duct: an investigation of multiple equilibrium positions. *Phys. Fluids* **18**, 031704.

CLARK, H. M. I. 1991 On the impact rate and impact energy of particles in a slurry pot erosion tester. *Wear* **147**, 165–183.

CLIFT, R., GRACE, J. R. & WEBER, M. E. 1978 *Bubbles, Drops, and Particles*. Academic.

CROCKETT, H. M. & HOROWITZ, J. S. 2010 Erosion in nuclear piping systems. *J. Pressure Vessel Technol.* **132**, 024501.

DREHER, S., KOCKMANN, N. & WOIAS, P. 2009 Characterization of laminar transient flow regimes and mixing in T-shaped micromixers. *Heat Transfer Engng* **30** (1–2), 91–100.

GOLDMAN, A. J., COX, R. G. & BRENNER, H. 1967 Slow viscous motion of a sphere parallel to a plane wall—I. Motion through a quiescent fluid. *Chem. Engng Sci.* **22**, 637–651.

GUHA, A. 2008 Transport and deposition of particles in turbulent and laminar flow. *Annu. Rev. Fluid Mech.* **40**, 311–341.

HALLER, D., WOIAS, P. & KOCKMANN, N. 2009 Simulation and experimental investigation of pressure loss and heat transfer in microchannel networks containing bends and T-junctions. *Intl J. Heat Mass Transfer* **52** (11), 2678–2689.

VAN HAREN, S.W. 2011 Testing DNS capability of OpenFOAM and STAR-CCM. Master's thesis, Delft University of Technology.

HIEMENZ, K. 1911 Die grenzschicht an einem in den gleichförmigen flüssigkeitsstrom eingetauchten geraden kreiszylinder (the boundary layer on a circular cylinder in uniform flow). *Dingl. Polytec. J.* **326**, 321–328.

HOMANN, F. 1936 Der einfluss grosser zähigkeit bei der strömung um den zylinder und um die kugel. *Z. Angew. Math. Mech.* **16**, 153–164.

JASAK, H. 1996 Error analysis and estimation for the finite volume method with applications to fluid flows. PhD thesis, University of London and Imperial College.

KOCKMANN, N. & ROBERGE, D. M. 2011 Transitional flow and related transport phenomena in curved microchannels. *Heat Transfer Engng* **32**, 595–608.

LEVY, A. V. 1995 *Solid particle erosion and erosion–corrosion of materials*. ASM International.

LEVY, A. V., JEE, N. & YAU, P. 1987 Erosion of steels in coal-solvent slurries. *Wear* **117**, 115–127.

LI, X., HUNT, M. L. & COLONIUS, T. 2012 A contact model for normal immersed collisions between a particle and a wall. *J. Fluid Mech.* **1**, 1–23.

LYNN, R. S., WONG, K. K. & CLARK, H. M. I. 1991 On the particle size effect in slurry erosion. *Wear* **149**, 55–71.

MARPLE, V. A. & LIU, B. 1974 Characteristics of laminar jet impactors. *Environ. Sci. Technol.* **8** (7), 648–654.

MCLAURY, B. S., WANG, J., SHIRAZI, S. A., SHADLEY, J. R. & RYBICKI, E. F. 1997 Solid particle erosion in long radius elbows and straight pipes. In *SPE Annual Technical Conference and Exhibition, 5–8 October 1997, San Antonio, Texas*. Society of Petroleum Engineers.

PASOL, L., MARTIN, M., EKIEL-JEZEWSKA, M. L., WAJNRYB, E., BLAWZDZIEWICZ, J. & FEUILLEBOIS, F. 2011 Motion of a sphere parallel to plane walls in a Poiseuille flow. Application to field-flow fractionation and hydrodynamic chromatography. *Chem. Engng Sci.* **66**, 4078–4089.

RADER, D. & MARPLE, V. A. 1985 Effect of ultra-Stokesian drag and particle interception on impaction characteristics. *Aerosol Sci. Technol.* **4** (1), 141–156.

RICHARDSON, J. F., COULSON, J. M., HARKER, J. H. & BACKHURST, J. R. 2002 *Chemical Engineering: Particle Technology and Separation Processes*. Butterworth-Heinemann.

RUBINOW, S. I. & KELLER, J. B. 1961 The transverse force on a spinning sphere moving in a viscous fluid. *J. Fluid Mech.* **11**, 447–459.

SHIVAMURTHY, R. C., KAMARAJ, M., NAGARAJAN, R., SHARIFF, S. M. & PADMANABHAM, G. 2010 Slurry erosion characteristics and erosive wear mechanisms of Co-based and Ni-based coatings formed by laser surface alloying. *Metall. Mater. Trans.* A **41**, 470–486.

SOMMERFELD, M. & HUBER, N. 1999 Experimental analysis and modelling of particle–wall collisions. *Intl J. Multiphase Flow* **25**, 1457–1489.

TOSCHI, F. & BODENSCHATZ, E. 2009 Lagrangian properties of particles in turbulence. *Annu. Rev. Fluid Mech.* **41**, 375–404.

TU, J. Y. 2000 Numerical investigation of particulate flow behaviour in particle–wall impaction. *Aerosol Sci. Technol.* **32**, 509–526.

TU, J. Y., YEOH, G. H., MORSI, Y. S. & YANG, W. 2004 A study of particle rebounding characteristics of a gas–particle flow over a curved wall surface. *Aerosol Sci. Technol.* **38**, 739–755.

VINCHURKAR, S., LONGEST, P. W. & PEART, J. 2009 CFD simulations of the Andersen cascade impactor: model development and effects of aerosol charge. *Aerosol Sci.* **40** (9), 807–822.

WONG, S. H., WARD, M. C. L. & WHARTON, C. W. 2004 Micro T-mixer as a rapid mixing micromixer. *Sensors Actuators B: Chemical* **100**, 359–379.

WOOD, R. J. K. & JONES, T. F. 2003 Investigations of sand–water induced erosive wear of AISI 304L stainless steel pipes by pilot-scale and laboratory-scale testing. *Wear* **255**, 206–218.

YANG, F. L. & HUNT, M. L. 2008 A mixed contact model for an immersed collision between two solid surfaces. *Phil. Trans. R. Soc.* A **366**, 2205–2218.

ZHANG, Y., REUTERFORS, E. P., MCLAURY, B. S., SHIRAZI, S. A. & RYBICKI, E. F 2007 Comparison of computed and measured particle velocities and erosion in water and air flows. *Wear* **263**, 330–338.

ZHAO, H. X., YAMAMOTO, M. & MATSUMURA, M. 1995 Slurry erosion properties of ceramic coatings and functionally gradient materials. *Wear* **186**, 473–479.